

## Plasmon excitations and accumulation layers in heavily doped InAs(001)

G. R. Bell and C. F. McConville\*

*Department of Physics, University of Warwick, Coventry, CV4 7AL, United Kingdom*

T. S. Jones

*Department of Chemistry, Imperial College of Science, Technology and Medicine, London, SW7 2AY, United Kingdom*

(Received 14 February 1996)

High-resolution electron-energy-loss spectroscopy (HREELS) has been used to study the (001) surface of degenerate *n*-type InAs grown by molecular-beam epitaxy and prepared either by As decapping or ion bombardment and annealing (IBA). The effects of temperature on the conduction-band electron plasmon excitation have been monitored with HREELS, and analyzed using dielectric theory in the framework of a three-layer model consisting of the bulk, an accumulation layer, and a carrier-free layer at the surface. Specific emphasis has been placed on the importance of the individual layer thicknesses, spatial dispersion, and plasmon lifetime in obtaining good theoretical agreement with the experimental spectra. The measured plasmon spatial dispersion coefficient for the decapped samples was found to agree with the predictions of the Thomas-Fermi model, but was significantly reduced for samples prepared by IBA. This is interpreted as a reduction in the average carrier velocity due to additional defect scattering. Samples prepared by both methods showed a sharp increase in plasmon damping at short wavelengths which is attributed to Landau damping. Ohmic damping of the plasmon at long wavelengths was found to be greater in the ion-bombarded samples, again due to additional defect scattering. IBA was also shown to increase the carrier concentration through the creation of donorlike defects. Neither the surface-state energy nor the surface-state density were found to be significantly affected by the IBA treatment. [S0163-1829(96)06928-7]

### I. INTRODUCTION

The (001) surface of InAs has for many years attracted significant interest because of its unusual electronic properties.<sup>1</sup> In particular, an electron accumulation layer is formed at the clean surface due to pinning of the Fermi level in the conduction band by intrinsic donorlike surface states.<sup>2,3</sup> This behavior contrasts with most other III-V semiconductor materials, such as InSb and GaAs, whose intrinsic and extrinsic surface states cause electron depletion in the near-surface region.<sup>4</sup> The high electron density at the InAs(001) surface makes possible several interesting device structures such as intersubband infrared detectors and nonalloyed Ohmic contacts.<sup>5</sup>

High-resolution electron-energy-loss spectroscopy (HREELS) has proved to be a very useful technique for studying the electronic properties of clean III-V semiconductor surfaces.<sup>6-19</sup> The surface-plasmon modes accessible using HREELS give valuable information about band bending, surface-state density, carrier concentration, and electron mobility. These modes are also of fundamental interest as excitations of an inhomogeneous electron gas. Much of this work to date has been directed towards GaAs(001) (Refs. 6 and 7) and InSb(001).<sup>8,9</sup> Extraction of the parameters mentioned above requires a detailed modeling of the near-surface region using the dielectric theory of HREELS.<sup>10-13</sup> For a surface depletion layer, a simple two-layer model is generally sufficient (a carrier-free layer on top of the bulk);<sup>13</sup> however, for an accumulation layer a more complex carrier profile is required.<sup>18,19</sup> This is due to the effect of the surface barrier on the conduction band electron wave functions: it is effectively infinite, and demands that the wave function be zero at the surface. This produces a carrier-free layer whose dimen-

sions are determined by the de Broglie wavelength of the electrons.<sup>18</sup> This layer is indistinguishable in HREELS from a depletion layer, although its origin is very different. Where there is electron accumulation, however, the carrier profile must rise from its bulk value and then fall to zero at the surface. The accumulation layer thickness is controlled by the screening length which is typically 30–100 Å for heavily doped semiconductors.

The surface reconstruction can strongly affect the intrinsic surface states, and hence the band bending. For example, it has been shown that for InAs(001), there is a significant difference in surface electron density between the (4×2) In-stabilized and (2×4) As-stabilized reconstructions.<sup>14</sup> In addition, the surface preparation method used can also influence the surface and the near-surface electronic properties. For InAs(001), cycles of low-energy ion bombardment and annealing (IBA) introduce donorlike defects in the near-surface region. These diffuse to a depth of at least 1000 Å, and the defect density depends strongly on the IBA conditions employed (i.e., ion energy, incidence angle, and annealing temperature).<sup>15</sup> A similar enhancement of electron concentration is found in the (001) surface inversion layer formed in *p*-type InAs,<sup>20</sup> and InAs quantum wells.<sup>21</sup> Thermal decapping of a protective arsenic layer provides an alternative method for surface preparation when the sample has been grown by molecular-beam epitaxy MBE.<sup>3</sup>

In this paper, HREELS data from degenerate InAs(001) (Si doped,  $n \sim 5 \times 10^{18} \text{ cm}^{-3}$ ) are presented and analyzed using semiclassical dielectric theory. The effects of different surface preparation procedures, including both decapping and IBA, have been studied along with the influence of the substrate temperature. The results are modeled using a three-layer system involving a semi-infinite bulk, an accumulation

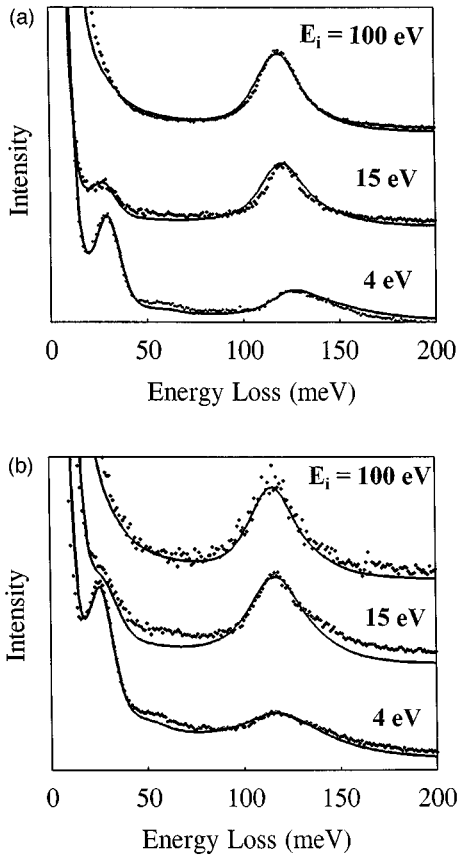


FIG. 1. Specular ( $\theta_i = \theta_s = 45^\circ$ ) HREEL spectra, recorded with  $E_i = 4, 15,$  and  $100$  eV, from decapped InAs(001) surfaces held at (a) 300 and (b) 500 K. The solid lines are the simulated spectra calculated for the three-layer model within the semiclassical dielectric theory using the parameters defined in Table I. All spectra are normalized to the specular elastic peak.

layer, and a carrier-free layer nearest the surface. The carrier statistics of highly degenerate InAs have been calculated using the rigid-band Kane model in order to derive the temperature dependence of the band bending.<sup>22</sup> Calculations of the electronic structure of the near-surface region are described and compared with the dielectric theory model. The influence on the HREEL spectra of plasmon damping, spatial dispersion, Fermi-level pinning at the surface, and surface preparation are discussed in detail.

## II. EXPERIMENT

The experiments were carried out in a conventional ultrahigh-vacuum chamber (base pressure  $\sim 1 \times 10^{-10}$  mbar) equipped with low-energy electron diffraction (LEED), HREELS, and a variable energy argon-ion gun for sputter cleaning. Sample heating was achieved by electron bombardment from a tungsten filament behind the sample, with the temperature measured by a chromel-alumel thermocouple in direct contact with the sample. While taking HREELS scans, the sample could be heated radiatively to between 500 and 600 K, with the chamber pressure kept at  $\sim 2 \times 10^{-10}$  mbar.

The HREEL spectrometer consists of a fixed monochromator and rotatable analyzer, both of the  $180^\circ$  hemispherical deflector type, with a four element entrance and exit lens

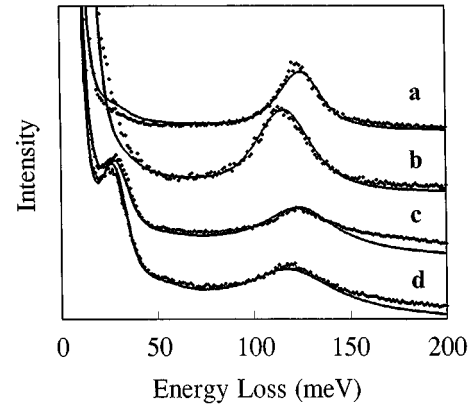


FIG. 2. Specular ( $\theta_i = \theta_s = 45^\circ$ ) HREEL spectra from IBA-treated InAs(001) surfaces recorded with (a)  $E_i = 100$  eV and 300 K, (b)  $E_i = 100$  eV and 600 K, (c)  $E_i = 6$  eV and 300 K, and (d)  $E_i = 6$  eV and 600 K. The solid lines are the simulated spectra calculated for the three-layer model within the semiclassical dielectric theory using the parameters defined in Table I. All spectra are normalized to the specular elastic peak.

system. Incident electron energies ( $E_i$ ) in the range 4–100 eV were used, and all spectra were collected in specular scattering geometry ( $\theta_i = \theta_s = 45^\circ$ ). The instrumental resolution was typically 10-meV full width at half maximum (FWHM) in the elastic peak, but was often degraded to  $\sim 15$  meV to improve count rates and reduce data collection times. The elastic peak FWHM and the overall background of the loss spectra were not affected by radiative heating. The positions of the loss peaks in the spectra are accurate to  $\pm 1$  meV.

The samples were grown by (MBE) in a separate system,<sup>23</sup> and were protected from atmospheric contamination during transfer to the HREELS system by an As capping layer.<sup>3</sup> This layer was removed in the HREELS chamber by annealing to 650 K for about 15 min, resulting in a somewhat disordered ( $4 \times 1$ ) LEED pattern. The samples were later subjected to two cycles of IBA using conditions chosen to minimize residual electronic damage (200–400-eV  $\text{Ar}^+$  at grazing incidence,  $\sim 3$ - $\mu\text{A}$  sample current for approximately 10 min, annealing to 650 K).<sup>15</sup> This procedure gave rise to a much sharper ( $4 \times 1$ ) LEED pattern.

## III. HREELS RESULTS

A series of normalized HREEL spectra, taken at various incident electron energies from clean InAs(001) samples following different surface preparations, are shown in Figs. 1 and 2. Figure 1(a) shows spectra ( $E_i = 4, 15,$  and  $100$  eV) from a decapped sample held at 300 K, whereas Fig. 1(b) shows the corresponding spectra from the same sample held at 500 K. The broad peak observed at  $\sim 120$  meV in all spectra is the conduction-band electron plasmon excitation. The intensity of this feature relative to the elastic peak increases at higher incidence energies, and the linewidth decreases. The peak position shifts to greater loss energy at low incidence energies, with a total shift of about 6 meV at both temperatures. All loss energies are about 5 meV lower at 500 K when compared with the corresponding spectra at 300 K.

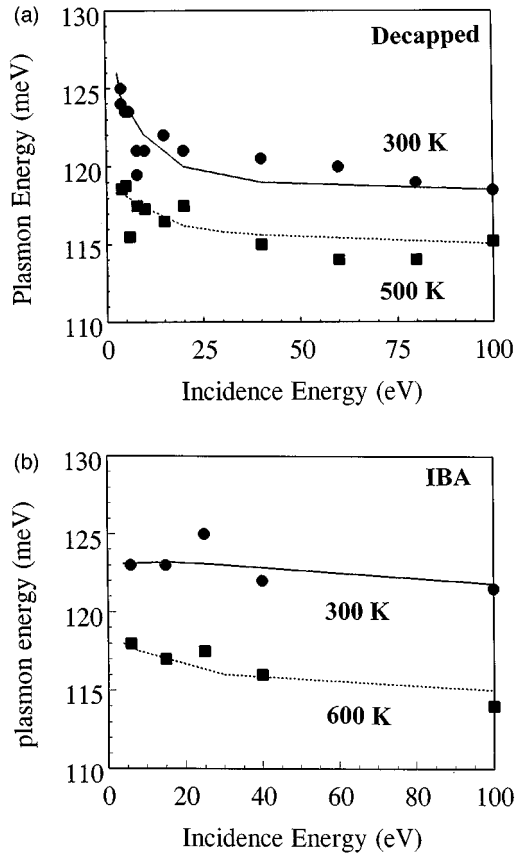


FIG. 3. The plasmon frequency plotted as a function of  $E_i$  for InAs(001) surfaces prepared by (a) decapping and (b) IBA. The points are the experimental data, whereas the solid and dashed lines are the fits based on the simulations at low and high temperatures, respectively.

There is also a noticeable increase in the asymmetry of the plasmon peak at low  $E_i$ , with the peak becoming less sharply defined on the high loss energy side. The sharper peak at  $\sim 27$  meV in the spectra recorded at low  $E_i$  is assigned to the surface optical phonon. This shows little change of loss energy, but its intensity falls off rapidly with increasing incidence energy. For energies greater than 15 eV, this loss peak is hardly detectable, except as a shoulder on the elastic peak (the instrumental resolution is, however, sufficient to resolve this peak in all spectra).

HREEL spectra taken from a sample treated by IBA, at temperatures of 300 and 600 K and incidence energies of 6 and 100 eV, are shown in Fig. 2. The phonon loss peak behaves in a very similar manner to that of the decapped samples. The plasmon peak, however, shows slightly less dispersion ( $\sim 4$  meV), and appears to be less asymmetric at low incidence energies.

The dispersion of the plasmon loss as a function of incident electron energy is shown in Fig. 3. Figure 3(a) shows data from a decapped sample at temperatures of 300 and 500 K. At both temperatures, the plasmon energy exhibits a significant decrease with increasing  $E_i$  before reaching approximately constant values (120 meV at 300 K and 115 meV at 500 K) for incident energies above 40 eV. In contrast, the plasmon energy observed in IBA-treated samples demonstrates little dispersion at both temperatures, although the

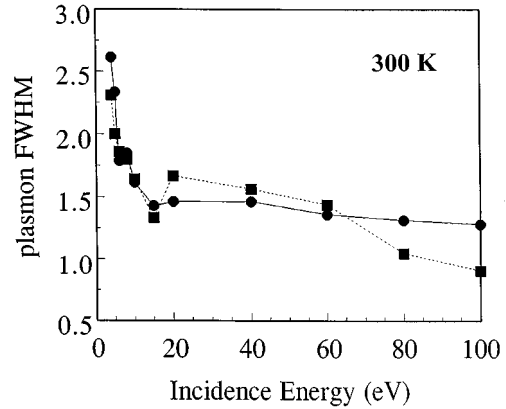


FIG. 4. The plasmon FWHM, normalized to the FWHM of the elastic peak, plotted as a function of  $E_i$  for InAs(001) surfaces prepared by decapping (circles) and IBA (squares) with the substrate temperature fixed at 300 K. The lines are included simply to guide the eye.

energy of the plasmon is higher in both cases (123 meV at 300 K and 117 meV at 600 K). It should be noted that in all cases the scatter of the points is greater at low incidence energies as the plasmon peak becomes broader and less well defined.

Information concerning the plasmon lifetime can, in principle, be extracted from measurements of the FWHM of the plasmon at different electron energies. The dependence of the plasmon FWHM (normalized to the FWHM of the elastic peak) on  $E_i$  is shown in Fig. 4. The two data sets correspond to samples (decapped and IBA treated) held at 300 K. Both plots show a sharp increase in plasmon width below about 8 eV, with a gradual decrease towards higher electron energies.

#### IV. ANALYSIS

This section deals with an analysis of the HREELS data presented in Sec. III, and is split into three parts. Section IV A introduces the basic ideas of semiclassical dielectric theory. Section IV B is concerned with the modeling of the various parameters required for the simulations. Finally, the simulations generated by the model are presented and discussed in Sec. IV C.

##### A. Dielectric theory of HREELS

Specular HREEL spectra were simulated using the approach developed by Lambin, Vigneron, and Lucas<sup>24</sup> in the framework of semiclassical dielectric theory. A classical loss spectrum is first calculated which includes only single losses. The scattering is described by a surface loss function, determined by the dielectric function of the target, and a kinematic factor which takes into account the classical scattering probability. Multiple losses (and gains) are then calculated quantum mechanically. In this second stage, the instrumental broadening is also taken into account by convolution with an instrumental response function which can be fitted to the elastic peak.

A three-layer model was used to analyze the HREELS data presented in Sec. III. This consists of a semi-infinite bulk, an accumulation layer in the middle, and a plasmon-

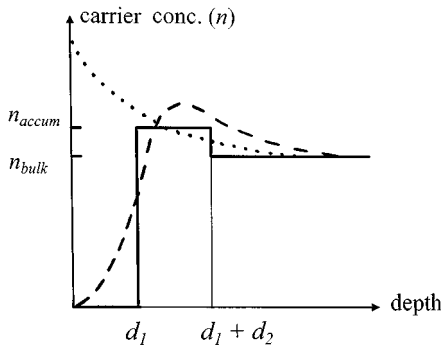


FIG. 5. A schematic diagram of the three-layer model used for the HREELS simulations. Also shown is a representation of the charge distribution near the InAs(001) surface, expected from classical (dotted) and quantum-mechanical (dashed) calculations, respectively.

free layer at the surface, with layer thicknesses  $d_3 = \infty$ ,  $d_2$ , and  $d_1$ , respectively (Fig. 5). The dielectric functions of the layers are given by

$$\epsilon_i(q, \omega) = \epsilon(\infty) \left[ 1 + \frac{\omega_{\text{ph}}^2}{\omega_{\text{TO}}^2 - \omega^2 - i\gamma\omega} - \frac{\omega_i^2}{\omega^2 - \beta_i^2 q^2 + i\omega/\tau_i} \right], \quad (1)$$

where  $q$  and  $\omega$  are the excitation wave vector and frequency, respectively,  $\epsilon(\infty)$  is the high-frequency dielectric constant (12.25 for InAs),<sup>25</sup> and  $\omega_{\text{ph}}$ ,  $\gamma$ , and  $\omega_{\text{TO}}$  are the phonon strength parameter, damping parameter, and frequency, respectively. These last three parameters were constant for all layers.<sup>26</sup>

The final term in Eq. (1) represents the plasmon response using a hydrodynamic description. The plasma frequencies  $\omega_i$  relate in the usual way to the effective mass ( $m^*$ ) and carrier concentrations ( $n_i$ ) by  $\omega_i^2 = n_i e^2 / \epsilon_0 \epsilon(\infty) m^*$ , with  $\omega_1$  set to zero in all calculations. The other parameters are the spatial dispersion ( $\beta_i$ ) in layers 2 (accumulation) and 3 (bulk), and the plasmon lifetime ( $\tau$ ), which is set equally in both layers. The derivation of  $\beta_i$  and  $\tau$  is discussed in Sec. IV B.

Apart from information concerning the spectrometer and the scattering conditions, the above variables completely define the simulation of the loss probability. These variables were adjusted to generate best-fit simulation curves over the whole electron energy range employed. For a given data set, only the plasmon lifetime was varied between electron energies and all other parameters were fixed over the whole incidence energy range. The plasmon peak width could not be fitted adequately without decreasing  $\tau$  at low incidence energies.

The parallel wave vector transfer  $q$  is related to  $E_i$  by

$$q = \left( \frac{m_e}{2\hbar^2} \right)^{1/2} \left( \frac{\hbar\omega}{E_i^{1/2}} \right) \sin\theta_i. \quad (2)$$

The effective probing depth of the electrons is then given approximately by the inverse of this wave vector.<sup>27</sup> Changes of probing depth with varying  $E_i$  affect the HREEL spectra because of the layered structure of the substrate, whereas changes of  $q$  with  $E_i$  affect the plasmon response directly through the spatial dispersion term. Both of these effects are

therefore mixed as the incidence energy is altered. This mixing and compensation between certain parameters (for example, increasing a plasma frequency while decreasing a dispersion coefficient) made it possible to generate superior fits for a single electron energy, but which was based on a model that generated very poor fits across the total-energy range. Fitting over the whole energy range was considered essential to produce a robust model for any particular data set.

## B. Model parameters

The simple rigid-band Kane model was used to describe the nonparabolic conduction band of *n*-type InAs.<sup>22</sup> This model has recently been tested for InAs heavily doped with Si,<sup>23</sup> and provides a good description of the varying effective mass for carrier concentrations less than  $2.7 \times 10^{19} \text{ cm}^{-3}$ , a condition satisfied in our experiments. The variation of the band gap is very significant over the temperature range used in these experiments, and has been described by Varshni's equation,<sup>28</sup> using fitting parameters derived from the literature.<sup>25</sup> The carrier concentration and other electron-gas parameters can then be calculated for various temperatures and over a range of degeneracies. The conduction band is highly degenerate at the doping levels used in these experiments, with the Fermi level lying several hundred meV above the conduction-band minimum.

It was assumed that the carrier concentration is independent of the temperature, with the strong variation in the position of the Fermi level and of the band gap with temperature accounting for the changes in the electron-gas properties in this system. HREELS studies of degenerate InSb, the conduction band of which can also be accurately described using the Kane model, have shown that changes in the measured plasmon response are due to shifts in the Fermi level with temperature, with no significant changes in the carrier concentration.<sup>13</sup> With this assumption, the Fermi level, the carrier velocity at the Fermi level, the effective mass at the Fermi level, the plasma frequency, and the Thomas-Fermi screening length can all be calculated at different temperatures. Figure 6 shows a plot of both the plasma frequency and Fermi-level position as a function of carrier concentration for the temperature ranges relevant to this study (300 and 600 K, respectively).

Values for the plasmon lifetime ( $\tau$ ) and spatial dispersion parameters ( $\beta_i$ ) are derived from complementary models. In the Drude model, Ohmic damping is related to the defect scattering rate of the electrons from both surface and bulk defects. This limits the plasmon lifetime which is related to the electron mobility according to  $\mu = e\tau/m^*$ . Additional plasmon damping occurs through the Landau mechanism, in which the damping arises from an intrinsic decay channel for the plasmon at short wavelengths. At wavelengths close to the screening length of the electron gas, the plasmon wave can decay into single-particle excitations. Although the model dielectric function of Eqn. (1) does not include single-particle excitations, their contribution to the energy-loss spectrum is small due to the low scattering probability in specular HREELS.<sup>29</sup>

The spatial dispersion parameter is described within the Thomas-Fermi model. For a degenerate electron gas,  $\beta$  is related to the velocity of the electrons at the Fermi level ( $v_f$ ) by  $\beta^2 = (\frac{3}{5})v_f^2$ . Values for the spatial dispersion coefficients

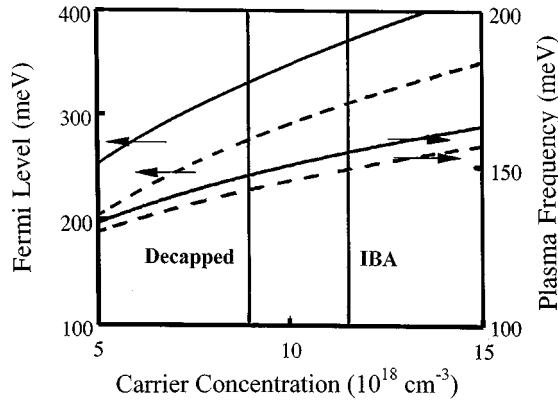


FIG. 6. The calculated plasma frequency and position of the Fermi level relative to the conduction-band minimum plotted as a function of carrier concentration for InAs at 300 K (solid line) and 600 K (dashed line). The values of the carrier concentration giving the best fits to the simulations for both decapped and IBA-treated samples are indicated in the figure by vertical lines.

were calculated from the Fermi velocities in the two plasma layers. The variation of  $\beta$  with carrier concentration at 300, 500, and 600 K is plotted in Fig. 7.

### C. HREELS simulations

Simulated HREEL spectra based on the three-layer model are shown in Figs. 1 and 2 along with the experimental data. For all incidence energies the simulated curves reproduce features of the plasmon and phonon peaks extremely well, with deviations being confined mainly to the background between loss peaks and at loss energies greater than the plasmon. The inclusion of a carrier-free layer is essential for good fit simulations. The relative phonon and plasmon intensities at low incident energies are strongly dependent on the plasmon-free layer thickness  $d_1$ . When the probing depth is significantly higher than  $d_1$ , the phonon is well screened and the plasmon dominates. This is shown clearly in Fig. 1, since no phonon mode is visible at 100 eV (probing depth  $\sim 450$  Å) despite adequate instrumental resolution. At low electron energies the phonon becomes much stronger due to the low effective probing depth ( $\sim 90$  Å at 4 eV). The phonon peak shape and position in the simulation were also dependent on the elastic peak parameters, since the phonon overlaps the elastic tail.

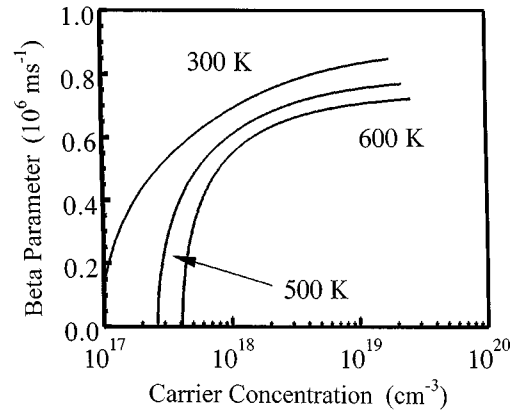


FIG. 7. Calculated values of the spatial dispersion parameter ( $\beta$ ) as a function of carrier concentration at 300, 500, and 600 K.

The plasmon energy dispersion is shown in Fig. 3. The simulations satisfactorily reproduce the observed dispersion for both temperatures and surface preparation methods, across the whole incidence energy range. Spatial dispersion has the greatest effect at low incidence energies. This can be seen in the upward dispersion of the plasmon (Fig. 3) and in the increased asymmetry and width of the plasmon peak (Figs. 1 and 2) at low  $E_i$ . The spectra could not be adequately simulated using a Drude model for the plasma (i.e., one neglecting spatial dispersion) even when other parameters (principally the plasma frequencies and plasmon damping) were adjusted to compensate. Despite direct plasmon peak broadening at low incidence energies due to the spatial dispersion term, the inclusion of additional broadening (by decreasing  $\tau$ ) was necessary for a good fit to the experimental spectra.

It should be noted that kinematic effects were significant in determining the position of the plasmon peak since the peak of the surface loss function did not coincide with the plasmon peak in most cases. The final peak position is determined by both the surface loss function and the kinematic factor. For broad loss features, the variation of the kinematic factor can have a significant effect on the observed peak position.<sup>30,31</sup> For the broad plasmon at low incidence energies, shifts of several meV were observed. The final best-fit parameters for the four experimental data sets discussed

TABLE I. Parameters for the three-layer model giving the best fits to the simulations of HREELS spectra recorded at different temperatures for InAs(001) surfaces prepared by decapping and IBA.

Parameter	300 K, decapped	500 K, decapped	300 K, IBA	600 K, IBA
$d_1$ (Å)	45	40	37	38
$d_2$ (Å)	60	75	30	65
$E_F$ (meV)	332	292	374	314
$V_{bb}$ (mV)	76	71	21	30
$\beta_3$ ( $10^6$ ms $^{-1}$ )	0.87	0.71	0.72	0.60
$n_{\text{bulk}}$ ( $10^{18}$ cm $^{-3}$ )	9	9	11.5	11.5
$n_{\text{accum}}$ ( $10^{18}$ cm $^{-3}$ )	13	14	14	13
$n_{ss}$ ( $10^{12}$ cm $^{-2}$ )	2.4	3.8	0.45	1.6
$\tau$ (ps)	0.052	0.050	0.028	0.034
$\mu$ (cm $^2$ V $^{-1}$ s $^{-1}$ )	1300	1220	670	720

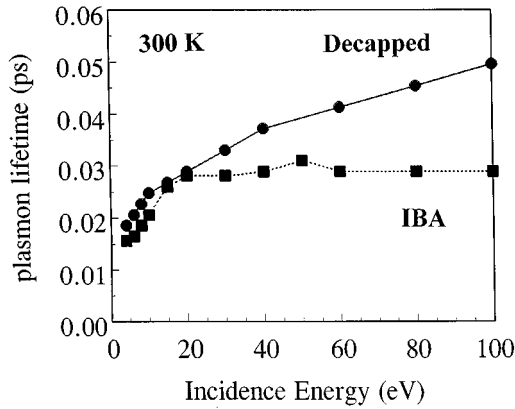


FIG. 8. The plasmon lifetime, extracted from the best-fit simulations and plotted as a function of  $E_i$ , for InAs(001) surfaces prepared by decapping and IBA at 300 K. The lines are included simply to guide the eye.

(IBA and decapped, room temperature, and high temperature) are summarized in Table I.

## V. DISCUSSION

The best-fit simulations for the decapped InAs samples were obtained with bulk plasma frequencies ( $\omega_3$ ) corresponding to bulk carrier concentrations of  $9.0 \times 10^{18} \text{ cm}^{-3}$  at both 300 and 500 K. For the IBA-treated samples, the bulk carrier concentration has a higher value of  $1.15 \times 10^{19} \text{ cm}^{-3}$  at both 300 and 600 K. This confirms that the carrier concentration is essentially independent of temperature, and that the downward shift of the plasmon frequencies at elevated temperature is due to the change of effective mass at the Fermi level (Fig. 6).

The higher carrier concentration in the sample prepared by IBA can be attributed to the generation of donorlike defects in the near-surface region as a consequence of the ion-bombardment process. This effect has previously been observed in InSb (Refs. 8 and 9) and InAs,<sup>15</sup> and is due to the diffusion of defects from the damaged surface region to a depth of the order of 1000 Å. The bombardment conditions strongly affect the resultant residual defect density, with grazing incidence and low ion energy producing the least damage in InAs.<sup>15</sup> Even when these conditions were employed, with a heavily doped sample, a significant change of carrier concentration was detected. With a maximum probing depth of only  $\sim 450$  Å, the enhanced carrier concentration appears bulklike. Subsequent Hall-effect measurements confirmed the observed increase in the bulk carrier concentration.

The increase in defect density can also affect the electron mobility and hence the plasmon lifetime. The lifetimes obtained from the simulations are shown in Fig. 8, as a function of incidence electron energy, for both IBA and decapped samples at a temperature of 300 K. At low  $E_i$  (and therefore high plasmon wave vectors), both plots show a sharp decrease in the plasmon lifetime. This corresponds to the onset (below about 10 eV) of strong, asymmetric broadening of the plasmon peak due to spatial dispersion, and is attributed to Landau damping. It should be noted that, although some broadening is introduced by spatial dispersion at these low

incidence energies, additional broadening is needed to fit the peaks. Ohmic damping of the plasmon is expected to dominate above  $E_i \sim 10$  eV, and significant differences can be seen in this region between the IBA and decapped samples (Fig. 8). The lifetime for the IBA-treated sample reaches a constant value of 0.028 ps at  $E_i \sim 20$  eV. In contrast, the lifetime for the decapped sample continues to increase steadily, reaching a value of 0.05 ps at the highest electron-beam energy used ( $E_i = 100$  eV).

This behavior can be explained by considering the combined effects of surface scattering, bulk defect scattering, and Landau damping. A semiquantitative analysis of the data shown in Fig. 8 was performed by using a simple sum rule to fit the three assumed damping contributions to the total damping obtained from the simulations, i.e.,

$$\frac{1}{\tau} = \frac{1}{\tau_L} + \frac{1}{\tau_D} + \frac{1}{\tau_S}, \quad (3)$$

where  $\tau_L$ ,  $\tau_D$ , and  $\tau_S$  are the lifetimes for Landau damping, bulk defect scattering, and surface scattering, respectively. To take into account the variation of the damping contributions with  $E_i$ , the plasmon damping curves were fitted using an equation of the form

$$\frac{1}{\tau} = \frac{a}{\sqrt{E_i}} + \frac{\sqrt{E_i}}{b}. \quad (4)$$

Both the Landau damping and surface-scattering contributions are contained in the parameter  $a$ . Landau damping is assumed to depend linearly on  $q$ , and hence inversely with  $E_i^{1/2}$ . Similarly, surface scattering depends inversely on the probing depth and therefore inversely with  $E_i^{1/2}$ . The bulk scattering contribution is assumed to increase linearly with probing depth, and is contained in the parameter  $b$ . The numerical fitting procedure allowed a free variation of  $a$  and  $b$  and produced excellent fits to both curves (Fig. 8). The resultant  $a$  parameters were nearly identical for both IBA and decapped samples, indicating that the total surface scattering and Landau damping contributions are very similar in each case. In contrast, the  $b$  parameter was found to be a factor 2.7 times greater in the IBA-treated sample. This represents a significantly increased bulk defect scattering rate. For the IBA sample, there is a very high density of defects as a result of the ion-bombardment process, at least equal to the additional donor density of  $2.5 \times 10^{18} \text{ cm}^{-3}$ . These defects dominate the plasmon damping, and are responsible for the observed increase in the bulk Ohmic damping.

The plasmon lifetime ( $\tau$ ) and Drude mobility ( $\mu$ ) for both sample preparation methods and for all temperatures are listed in Table I (note that the varying effective mass is taken into account when calculating mobilities). These values are based on the 100-eV HREEL spectra, and therefore represent almost entirely Ohmic damping due to bulk defects. The defect and surface scattering rates are not expected to vary strongly with temperature in the range 300–600 K. Similarly, Landau damping at low incidence energies is expected to be nearly independent of temperature. No significant variation in the plasmon lifetime with temperature was observed.

The best fits in the HREELS simulations for the decapped samples (Fig. 1) were obtained with  $\beta$  values of  $0.87 \times 10^6$

$\text{ms}^{-1}$  at 300 K and  $0.71 \times 10^6 \text{ms}^{-1}$  at 500 K. Significantly larger values produced extreme damping of the plasmon and too great a degree of dispersion, whereas smaller values failed to generate the required asymmetry and dispersion. The implication is that the Thomas-Fermi model correctly describes the spatial dispersion coefficient for samples prepared by decapping, in agreement with recent HREELS studies on GaAs(001).<sup>7</sup>

In a previous HREELS study of decapped InAs(001), Egdell *et al.*<sup>3</sup> concluded that the Thomas-Fermi model overestimates the spatial dispersion coefficient due to neglect of electron correlation and exchange interactions. In their work, HREEL spectra were analyzed by fitting a surface-plasmon-like dispersion curve to the plasmon energy data points, with the doping level of the sample ( $n \sim 8 \times 10^{18} \text{cm}^{-3}$ ) chosen to give an approximately flatband behavior. This analysis ignored both the plasmon-free layer and the kinematic effects of scattering on the plasmon peak position, resulting in a much lower fitted  $\beta$  parameter of  $0.5 \times 10^6 \text{ms}^{-1}$ . This discrepancy is almost certainly due to neglect of the carrier-free layer, which has a strong downward influence on the plasmon energy at low probing depths.

Recent HREELS studies of ion-bombarded InSb(001) showed that the spatial dispersion coefficient was lower than the value calculated from the Thomas-Fermi model.<sup>13</sup> It was suggested that the high defect density as a result of the ion-bombardment process reduces the spatial dispersion coefficient by increasing the scattering rate of carriers, such that their mean velocity is significantly lower than  $v_f$ . The best fits in the HREELS simulations for the IBA-treated InAs(001) samples (Fig. 2) were obtained with  $\beta$  values of  $0.72 \times 10^6 \text{ms}^{-1}$  at 300 K and  $0.6 \times 10^6 \text{ms}^{-1}$  at 600 K. These are significantly less than the calculated values ( $0.85 \times 10^6$  and  $0.72 \times 10^6 \text{ms}^{-1}$  at 300 and 600 K, respectively, as shown in Fig. 7), supporting the hypothesis that additional defects reduce the average carrier velocity and hence the spatial dispersion effect.

The free-carrier profile near the InAs(001) surface depends on the screening length of the electron gas, the de Broglie wavelength of the electrons, and the band bending. A full calculation of the profile, based on a simultaneous solution of the Schrödinger and Poisson equations for the degenerate electron gas in a highly nonparabolic conduction band, has not been attempted. A schematic profile of the expected charge distribution is shown in Fig. 5. If a classical model is used for the space charge, and the effects of the surface barrier are ignored, the carrier density increases all the way up to the surface.<sup>32</sup> However, when the effect of the surface barrier on the conduction-electron wave functions is considered in a quantum-mechanical model, the carrier density falls to zero at the surface over a length given approximately by half the average de Broglie wavelength.<sup>12,18</sup> The carrier concentration then rises in the accumulation layer before diminishing more slowly back to the bulk value.

The de Broglie wavelength was calculated to be 70–90 Å and this compares well with the values for  $d_1$  obtained from the three-layer model (see Table I). The accumulation layer thickness ( $d_2$ ) is expected to be governed by both the band bending and the Thomas-Fermi screening length. This screening length was calculated to be 35–40 Å for all of the four cases considered. In order to take account of the band

bending, however, a classical calculation was performed. This calculation was based on an approximate but analytical solution to Poisson's equation, taking into account the non-parabolicity and the degeneracy of the conduction band, and accurate for weak band bending ( $<100 \text{meV}$ ). This indicates that the decay length of the space charge was approximately 50–60 Å for a band bending of 80 meV, and 30–40 Å for a band bending of 30 meV. The values of  $d_2$  used in the best-fit simulations are in reasonable agreement with these figures.

It is clear from the simulations presented here that the inclusion of an accumulation layer is essential to fit all of the four data sets. This indicates that downward band bending occurs at the surface in all cases due to the existence of donorlike surface states. Previous HREELS and ultraviolet photoemission measurements on decapped InAs(001) indicate that these states lie some 250–300 meV above the conduction-band minimum.<sup>3</sup> The band bending at the surface can be estimated by calculating the Fermi level in the accumulation layer and in the bulk, based on the carrier concentrations. For the decapped samples, this gives 76 and 71 meV for temperatures of 300 and 500 K, respectively. For the samples prepared by IBA, values of 31 and 20 meV are obtained for temperatures of 300 and 600 K, respectively. These measurements indicate downward band bending of  $\sim 75 \text{meV}$  at a carrier concentration of  $9 \times 10^{18} \text{cm}^{-3}$ , in contrast to the measurements of Egdell *et al.*,<sup>3</sup> which cite flatband behavior for a bulk carrier concentration of  $8 \times 10^{18} \text{cm}^{-3}$ . In our work the bands are nearly flat with a measured carrier concentration of  $1.15 \times 10^{19} \text{cm}^{-3}$ . Potential sources for this discrepancy include the inaccuracy of previous photoemission measurements<sup>3</sup> or the assumed abruptness in the interfaces used in our three-layer dielectric model.

The intrinsic surface states of the InAs(001) surface are responsible for the formation of the accumulation layer. The number of active surface states can be derived from the three-layer model by simply calculating the additional carrier density in the accumulation layer. It can be seen from Table I that with a bulk Fermi level of 292 meV, there is a high density of active surface states ( $n_{ss} = 3.8 \times 10^{12} \text{cm}^{-2}$ ) with significant band bending. When the bulk Fermi level is increased to 374 meV, this density drops by almost an order of magnitude (to  $n_{ss} = 4.5 \times 10^{11} \text{cm}^{-2}$ ). At this point the situation is almost flatband, with few available conduction-band states for electrons from ionized surface states. This indicates that the surface states lie somewhere between these two energy levels at around 320 meV. This figure is approximate, since it is based on a very simple single accumulation layer model for the carrier distribution. It is, however, in reasonable agreement with previous estimates.<sup>2,3</sup> For bulk Fermi levels of 314 meV (IBA, 600 K) and 332 meV (decapped, 300 K), the thermal broadening of the Fermi distribution is of similar magnitude to the band bending, making the degree of activation of the surface states difficult to estimate. However, both show intermediate surface-state densities ( $1.6$  and  $2.4 \times 10^{12} \text{cm}^{-2}$ ). In particular, there is no evidence for a significant change of surface-state density between the decapped and IBA-treated samples within the limitations of the three-layer analysis.

Previous work on InAs(001) surfaces, grown by MBE and analyzed *in situ* by HREELS, suggested that the surface-state

density is correlated with the surface reconstruction.<sup>14</sup> It was found that the In-terminated ( $4\times 2$ ) surface had a surface-state density of  $\sim 5\times 10^{11}$  cm<sup>-2</sup>, whereas the As-terminated ( $2\times 4$ ) surface had a surface-state density of  $\sim 1\times 10^{12}$  cm<sup>-2</sup>. In our measurements, the surfaces exhibited a ( $4\times 1$ ) reconstruction for both decapped and ion-bombarded samples, strongly suggesting In termination with one-dimensional disorder in the direction of the In dimers. The surface-state density is rather high ( $n_{ss}=3.8\times 10^{12}$  cm<sup>-2</sup>), but is most likely overestimated by the use of the three-layer model, which uses a simple rectangle to model the accumulation layer. A more realistic profile for the accumulation layer may well result in a lower value for the calculated surface-state density.

## VI. CONCLUSIONS

HREELS has been used to study the (001) surface of degenerate *n*-type InAs prepared both by IBA and As decapping. The effects of surface preparation methods and the sample temperature on the plasmon damping, carrier profile, and spatial dispersion have been investigated. These parameters have been derived from HREELS data simulated using a three-layer dielectric model together with model calculations. The layer thicknesses used in the model agreed reasonably well with the calculated screening length, de Broglie wavelength, and space-charge decay length. The measured

plasmon spatial dispersion coefficient for the decapped samples ( $0.87$  and  $0.71\times 10^6$  ms<sup>-1</sup> at  $300$  and  $500$  K, respectively) was found to agree with the predictions of the Thomas-Fermi model, but was significantly reduced for samples prepared by IBA ( $0.72$  and  $0.60\times 10^6$  ms<sup>-1</sup> at  $300$  and  $600$  K, respectively). This is interpreted as a reduction in the average carrier velocity due to additional scattering from defects introduced by the IBA treatment. Additional plasmon damping at short wavelengths (Landau damping) has also been observed. Ohmic damping at long wavelengths was found to be greater in the ion-bombarded samples, again attributed to additional defect scattering. In all cases IBA was shown to increase the bulk carrier concentration significantly and to decrease the electron mobility through the creation of donorlike defects.

## ACKNOWLEDGMENTS

We thank Dr. W. T. Yuen and Professor R. A. Stradling (Imperial College) for the provision of the MBE-grown InAs samples used in this work. Dr. A. R. Avery is also thanked for performing the Hall measurements. Financial support for this work was provided by the Engineering and Physical Sciences Research Council (EPSRC), U.K. under Contract No. GR/J83543. The provision of an EPSRC studentship for G.R.B. is also acknowledged.

\*FAX: ++44-(0)1203-692-016.

Electronic address: C.F.McConville@warwick.ac.uk

<sup>1</sup>P. D. Wang, S. N. Holmes, T. Le, R. A. Stradling, I. T. Ferguson, and A. G. de Oliveira, *Semicond. Sci. Technol.* **7**, 767 (1992).

<sup>2</sup>Y. Yamaguchi and Y. Horikoshi, *Phys. Rev. B* **51**, 9836 (1995).

<sup>3</sup>R. G. Egdell, S. D. Evans, R. A. Stradling, Y. B. Li, S. D. Parker, and R. H. Williams, *Surf. Sci.* **262**, 444 (1992).

<sup>4</sup>W. Mönch, *Semiconductor Surfaces and Interfaces* (Springer-Verlag, Berlin, 1993), and references therein.

<sup>5</sup>J. M. Woodall, J. L. Freeouf, G. D. Petit, T. Jackson, and P. Kirchner, *J. Vac. Sci. Technol.* **19**, 626 (1981).

<sup>6</sup>Z. J. Gray-Grychowski, R. G. Egdell, B. A. Joyce, R. A. Stradling, and K. A. Woodbridge, *Surf. Sci.* **186**, 482 (1987).

<sup>7</sup>V. Polyakov, A. Elbe, and J. A. Schäfer, *Appl. Phys. A* **60**, 567 (1995).

<sup>8</sup>T. S. Jones, M. Q. Ding, N. V. Richardson, and C. F. McConville, *Appl. Surf. Sci.* **45**, 85 (1990).

<sup>9</sup>T. S. Jones, M. Q. Ding, N. V. Richardson, and C. F. McConville, *Surf. Sci.* **247**, 1 (1991).

<sup>10</sup>A. A. Lucas, J. P. Vigneron, Ph. Lambin, P. A. Thiry, M. Liehr, J. J. Pireaux, and R. Caudano, *Int. J. Quantum Chem. Symp.* **19**, 687 (1986).

<sup>11</sup>T. Inaoka and I. Chihara, *Surf. Sci.* **208**, 71 (1989).

<sup>12</sup>T. Inaoka, D. M. News, and R. G. Egdell, *Surf. Sci.* **186**, 290 (1987).

<sup>13</sup>T. S. Jones, M. O. Schweitzer, N. V. Richardson, G. R. Bell, and C. F. McConville, *Phys. Rev. B* **51**, 17 675 (1995).

<sup>14</sup>M. Noguchi, K. Hirakawa, and T. Ikoma, *Phys. Rev. Lett.* **66**, 2243 (1991).

<sup>15</sup>G. R. Bell, C. F. McConville, and T. S. Jones, *Appl. Surf. Sci.* (to be published).

<sup>16</sup>M. G. Betti, U. Del Pennino, and C. Mariani, *Phys. Rev. B* **39**, 5887 (1989).

<sup>17</sup>Y. Chen, S. Nannarone, J. Schaefer, J. C. Hermanson, and G. J. Lapeyre, *Phys. Rev. B* **39**, 7653 (1989).

<sup>18</sup>D. H. Ehlers and D. L. Mills, *Phys. Rev. B* **36**, 1051 (1987).

<sup>19</sup>Y. Chen, J. C. Hermanson, and G. J. Lapeyre, *Phys. Rev. B* **39**, 12 682 (1989).

<sup>20</sup>M. F. Millea, A. H. Silver, and L. D. Flesner, *Thin Solid Films* **56**, 253 (1979).

<sup>21</sup>P. H. C. Magnée, S. G. den Hartog, B. J. van Wees, W. van de Graaf, and G. Borghs, *Appl. Phys. Lett.* **67**, 3569 (1995).

<sup>22</sup>E. O. Kane, *J. Phys. Chem. Solids* **1**, 249 (1957).

<sup>23</sup>Y. B. Li, R. A. Stradling, T. Knight, J. R. Birch, R. H. Thomas, C. C. Phillips, and I. T. Ferguson, *Semicond. Sci. Technol.* **8**, 101 (1993).

<sup>24</sup>Ph. Lambin, J. P. Vigneron, and A. A. Lucas, *Comput. Phys. Commun.* **60**, 351 (1990).

<sup>25</sup>*Semiconductors, Physics of Group IV Elements 2nd III-V Compounds*, edited by K. H. Hellwege and O. Madelung, Landolt-Börnstein, New Series, Group III, Vol. 17, Pt. a (Springer-Verlag, Berlin, 1982).

<sup>26</sup>P. A. Thiry, J. L. Longueville, J. J. Pireaux, R. Caudano, H. Munekata, and M. Liehr, *J. Vac. Sci. Technol. A* **5**, 603 (1987).

<sup>27</sup>H. Ibach and D. L. Mills, *Electron Energy Loss Spectroscopy and Surface Vibrations* (Academic, New York, 1982).

<sup>28</sup>Y. P. Varshni, *Physica* **34**, 149 (1967).

<sup>29</sup>H. Yu and J. C. Hermanson, *Phys. Rev. B* **40**, 11 851 (1989).

<sup>30</sup>R. E. Palmer, J. F. Annett, and R. F. Willis, *Phys. Rev. Lett.* **58**, 2490 (1987).

<sup>31</sup>P. J. Chen, J. E. Rowe, and J. T. Yates, Jr., *Phys. Rev. B* **50**, 18 134 (1994).

<sup>32</sup>F. Stern, *Crit. Rev. Solid State Sci.* **4**, 499 (1974).